

Ultimate Merging at $z \sim 0.1$

Daniel Maschmann^{1,2}, Anne-Laure Melchior¹

¹ Sorbonne Université, LERMA, Observatoire de Paris, PSL research university, CNRS, F-75014, Paris, France

² RWTH Aachen University, Institute for Philosophy of Science and Technology, Aachen, Germany
e-mail: Daniel.Maschmann@rwth-aachen.de, A.L.Melchior@obspm.fr

Received April ?, 2019; accepted ?

ABSTRACT

We present a study of 58 double-peaked emission line galaxies for which one of the components is suppressed in [OIII] λ 5008 or significantly weaker than the other one. Accordingly, the two components are classified differently in the BPT diagram. We show that the strong [OIII] component coincides with the stellar velocity and the suppressed component is off-centred in 66% of the galaxies, while in 12% of them it is the opposite. The analysis of their morphology reveals that about half of the sample is composed of S0, the rest is composed in equal part of mergers and late-type galaxies. We discuss that these characteristics exclude rotating discs and suggest different stages of merging. It is possible that the number of mergers is underestimated if the double nuclei are not resolved. Tidal features are detected in the outskirts of some S0 galaxies. This high fraction of S0 is surprising, as in addition most of the galaxies are isolated and the others in small groups. All these galaxies, hosting an AGN component, are massive, lie on the star forming sequence, and exhibit an enhanced star formation in their centre. While we cannot exclude outflows, these galaxies exhibit a spectra, which do not correspond to usual outflow observations characterised by high gas velocities, and the standard deviations of the two peaks are comparable. In parallel, these characteristics are compatible with ultimate stages of galaxy merging, where the two nuclei are too close to be detected or dynamical disturbances might be present in post-mergers like massive S0.

Key words. galaxies: kinematics and dynamics, galaxies: interactions, galaxies: evolution, galaxies: irregular, techniques: spectroscopic, methods: data analysis

1. Introduction

The building-up of galaxies is currently understood as a co-evolution of the star formation (SF), usually strong in the central parts, and the accretion activity of the central black hole (Madau & Dickinson 2014). While galaxy interactions can trigger SF (Mihos & Hernquist 1994, 1996; Bellocchi et al. 2013), gas accretion is not negligible (Kereš et al. 2005; Sancisi et al. 2008). In the local Universe, interactions and minor/major mergers do not necessarily enhance SF (e.g. Bergvall et al. (2003); Bell et al. (2005); Di Matteo et al. (2007)), but they can also drive gas towards the centre, fuel the nuclear black hole, enhancing active galactic nuclei (AGN) activity and feedback (Croton et al. 2006; Springel et al. 2005). Major mergers are definitely providing the largest starbursts (Sanders & Mirabel 1996), but they are rare, and their influence on the total cosmic SF is low (Di Matteo et al. 2007; Robaina et al. 2009). Galaxy mergers are usually identified on their optical morphology. Wide field observations connect enhanced AGN and starburst activities with interactions in galaxy pairs (Patton et al. 2013; Satyapal et al. 2014).

In this letter, we investigate a galaxy sample based on a spectroscopic selection. Relying on the RCSED catalogue from Chilingarian et al. (2017), Maschmann et al. (in prep.) have performed an automatic selection of about 5000 galaxies from the SDSS catalogue (Strauss et al. 2002), exhibiting double-peak emission lines. We study here 58 such double-peak galaxies, whose peaks exhibit two different Baldwin, Phillips & Terlevich (BPT) diagnostics: AGN/SF, AGN/composite or composite/SF. Previous works on double-peaked emission-lines, motivated by dual or offset AGNs, were restricted to AGN lines. Different works identified galaxy mergers and AGN outflows (Comerford

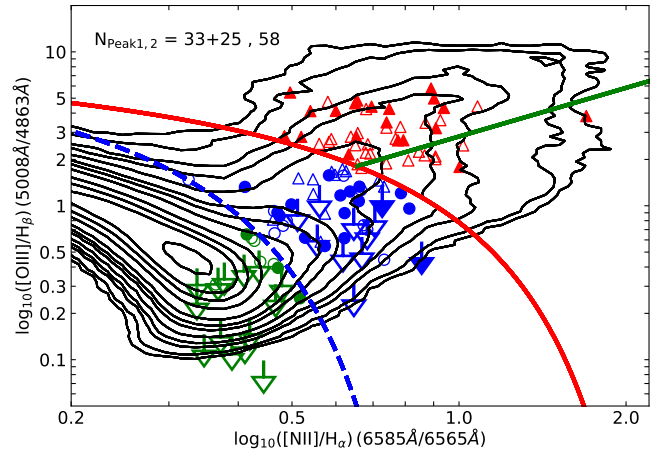


Fig. 1. BPT diagnostic diagram (Kewley et al. 2006) with topological classification based on Kauffmann et al. (2003), Kewley et al. (2001) and Schawinski et al. (2007). We show the two components of the double-peak galaxies: 58 triangles represent the strong [OIII] component and 33 circles the weaker [OIII] component. We display the 25 upper limits with an arrow for those galaxies, which have a $\text{SNR} < 3$ suppressed component. We highlight galaxies with a off-centred weak [OIII] line with an empty marker (see Sect. 2.3).

et al. 2018; Liu et al. 2018; Nevin et al. 2018; Müller-Sánchez et al. 2015). As discussed in Ge et al. (2012), beside dual AGN, double-peaked emission lines can correspond to several configurations difficult to disentangle: rotating disk, gas outflow or different gas components due to a galaxy merger. In this work, we

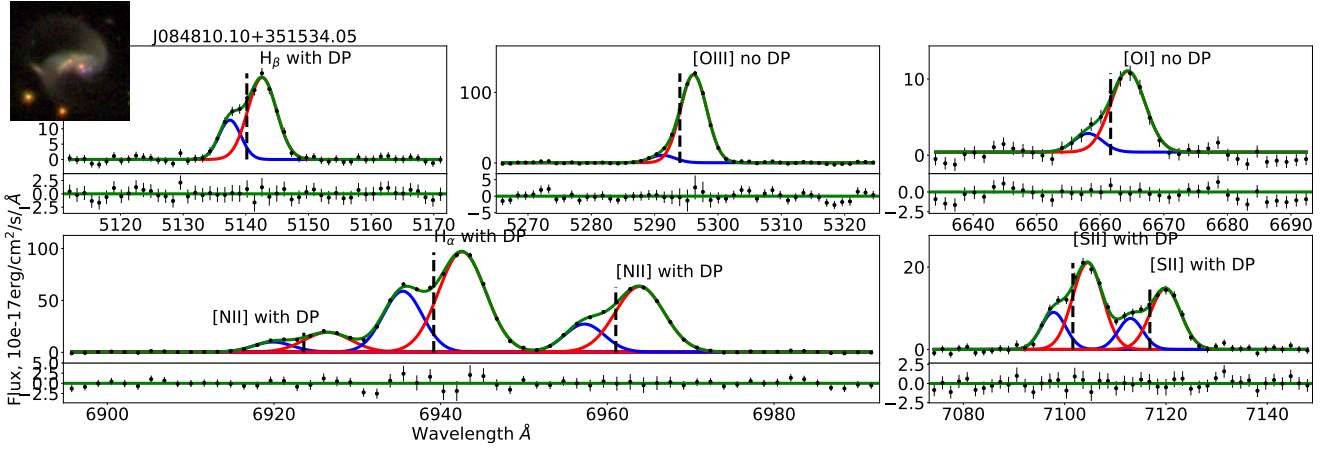


Fig. 2. Emission lines of one double-peak galaxy classified as merger (Domínguez Sánchez et al. 2018) at $z=0.057$, namely $H\beta\lambda 4863$, $[OIII]\lambda 5008$, $[OI]\lambda 8446$, $[NII]\lambda 6586$, $H\alpha\lambda 6565$, $[NII]\lambda 6586$, $[SII]\lambda 6718$ and $[SII]\lambda 6733$. We display on the top left, the SDSS snap-shot. Each displayed line is fitted with a double Gaussian function (with velocities fixed with the stacked spectra) as displayed by blue and red lines. The black dashed line indicates the position of the stellar velocity of the host galaxy, computed by Chilingarian et al. (2017). As in Maschmann et al. (in prep), we indicate emission lines with a confirmed double-peak "with DP" (resp. "no DP"). Beside SNR constraints, the non-detection corresponds to a line weaker than a factor 3.

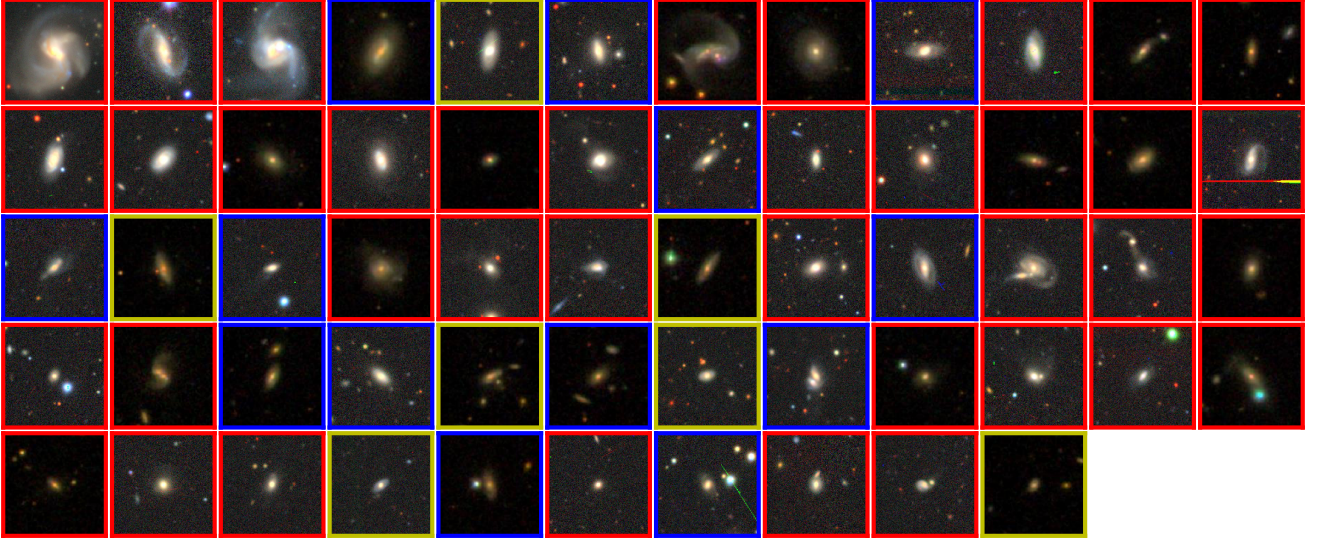


Fig. 3. Galaxy $150'' \times 150''$ snapshots sorted by redshift. We show the Legacy Survey snapshots (Dey et al. 2019) if available otherwise we display the SDSS snapshots (Strauss et al. 2002). We highlight galaxies which are classified with a centred strong (resp. weak) $[OIII]\lambda 5008$ component on the stellar velocity with a red (resp. yellow) and those with symmetrical kinematics with blue frames as described in Sect. 2.3.

focus on double-peak emission-line galaxies with a high signal-to-noise ratio (SNR) in all lines, but with one of the $[OIII]\lambda 5008$ components absent or significantly weaker than the other one. As further argued throughout this letter, we do not expect rotating discs exhibiting such a pattern, which favours the merging and possibly outflow scenarios. In Sect. 2, we present the spectroscopic selection of the galaxy sample, their host properties, the estimated star formation and their environment. In Sect. 3, we discuss the results. A cosmology of $\Omega_m = 0.3$, $\Omega_\Lambda = 0.7$ and $h = 0.7$ is assumed in this work.

2. Data analysis: host properties of merger candidates

Relying on the RCSED catalogue (Chilingarian et al. 2017), a single and a double Gaussian function are fitted to the emission-lines and several selection criteria have been applied. We stacked

all fitted emission lines and introduced a global peak position and velocity dispersion (σ) for each peak. ϕ_1 (resp. ϕ_2) corresponds to the flux of the blueshifted (resp. redshifted) component. The catalogue finally provides parameters of the fitted double Gaussian function for the different optical lines. We restrict the analysis to the $H\beta\lambda 4863$, $[OIII]\lambda 5008$, $H\alpha\lambda 6565$ and $[NII]\lambda 6586$ emission-lines.

2.1. Spectroscopic selection and classification

We focus here on galaxies with (1) a $H\alpha\lambda 6565$ flux ratio between the two components in the range $1/2 < \phi_1/\phi_2 < 2$ and (2) an $[OIII]\lambda 5008$ flux ratio below $1/3$ or above 3 . We also require a signal-to-noise ratio (SNR) larger than 10 for the $[OIII]\lambda 5008$ line. We hence select galaxies with a well-defined double-peak structure in the $H\alpha\lambda 6565$ line, but suppressed in $[OIII]\lambda 5008$. At this stage, we select 123 galaxies. We then classify each emission

line component individually with a BPT diagram (Baldwin et al. 1981; Kewley et al. 2006) and select the galaxies with two different classifications. We finally get 58 galaxies as displayed in Figure 1. The weaker components are situated in the composite and star forming regions. The components with the higher [OIII] flux are clearly associated with AGN/LINER activity but for 11 located in the composite region. We later refer to the two components as the weak [OIII] and the strong [OIII] components. Examples of spectra of galaxies thus selected are displayed in Figure 2 and Figure A.1.

We also classify the sample with the WHAN diagram shown in Figure A.2. While a shift is observed between the two components, there are only 9 out of 58 galaxies with AGN/SF classification. The BPT-AGN are classified strong and weak AGN in the WHAN diagnostics. The BPT-based composite and star forming classifications are more ambiguous. However, the WHAN diagram (Cid Fernandes et al. 2010) based on equivalent widths is biased if there is an AGN in one component as the continuum of both components will be affected.

In Table A.1, we list the properties of the 58 galaxies sorted by redshift.

2.2. Morphology

Our selected sample is composed of galaxies with redshifts in the range 0.04-0.17, corresponding to a SDSS 3" fiber diameter between 2 and 10 kpc. The mean stellar masses are around $\log_{10}(M/M_{\odot}) \sim 11$ (Kauffmann et al. 2003). Relying on a machine-learning-based morphological classification (Domínguez Sánchez et al. 2018) and a visual correction when required, we classify this sample as 15 (26%) merger, 16 (28%) late-type (LTG), 1 (2%) early type (ETG) and 26 (45%) S0 galaxies. Only one galaxy has been (mis-)classified as elliptical, and it might be a S0. Several galaxies were mis-classified by machine-learning-based morphological classification, e.g. close double nuclei were missed. We show snapshots in Figure 3. Beside galaxies classified mergers, many tidal features can be observed even around S0 galaxies. This can be compared to the work of Eliche-Moral et al. (2018), who show that S0 galaxies resulting from major/minor mergers exhibit tidal features in their outskirts. Last, one can note the large fraction of S0 galaxies compared to the usual fraction observed in magnitude limited samples e.g. 11% in Shapley-Ames Catalog (van den Bergh 2009).

2.3. Kinematics

The velocity differences between the two peaks are between 215 and 415 km s^{-1} . These values correspond to the upper range of the Tully-Fisher relation expected according to the stellar masses (McGaugh et al. 2000).

We then compare the velocity of each emission-line component with the stellar velocity. We compute the ratio of $\Delta V = v_{\text{peak}} - v_*$ the difference between the individual peak position v_{peak} and the stellar velocity v_* of the host galaxy, to the velocity dispersion σ of the component. In Figure 4, we display these ratios for the weak [OIII] component as a function of those of the strong [OIII] component. We then study if one of the two peaks is centred on the same velocity as the stars or not. We classify galaxies with off-centred strong (resp. weak) [OIII] components as those showing a velocity offset in this component, larger than at least 1σ from the stellar velocity. We clearly see that for the majority (66%) of these galaxies, the position of the

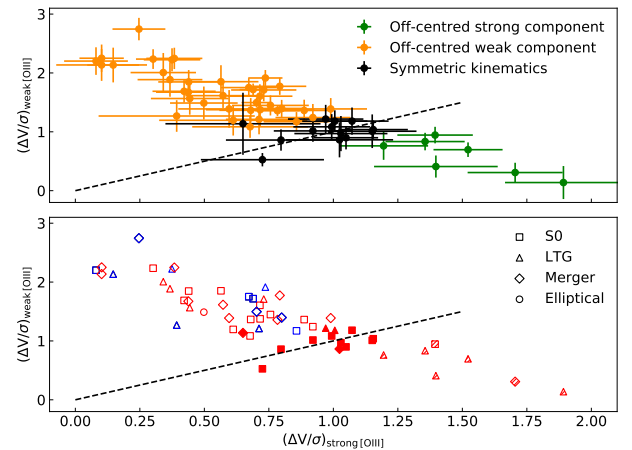


Fig. 4. Velocity offsets of the two emission-line components relative to the stellar velocity of the host galaxy in units of their velocity dispersion σ . The two panels show the exact same points. On the y-axis (resp. x-axis), we display the relative offset of the weak [OIII] (strong [OIII]) component. In the upper panel, we compute error-bars and colour-code off-centred strong (resp. weak) [OIII] lines in green (resp. orange) and symmetric kinematics in black. In the lower panel, we encode the morphological classification with different marker styles and the BPT classification of the strong [OIII] component (see Figure 1) with the colour.

strong [OIII] peak is closer to the stellar velocity than for the weak [OIII] peak. This comprises also all galaxies with a strong [OIII] component classified as composite (see Sect. 2.1). But we find also 7 galaxies showing an off-centred strong [OIII] component. The latter are mostly classified as LTG (5), and the remaining are respectively one merger and one S0 galaxy. Last, we also find that 13 galaxies (22%) have the stellar velocity centred between the two peaks. The majority (9) of those are S0 galaxies, the others are 2 LTG and 2 mergers.

2.4. Environment

Following Yang et al. (2007), we estimate the number of identified neighbours, associated to each galaxy of the studied sample. The majority of the galaxies (67%) is composed of isolated galaxies with no identified counterparts, 46% of those are classified S0, 21% mergers and 31% late-type galaxies. 12 galaxies are located in small groups composed of 2 to 5 galaxies. 3 (25%) are late-type, 5 (41%) mergers and 4 (33%) S0 galaxies. Only one S0 galaxy is located in a small cluster with 27 counterparts. Last, 6 galaxies (10%) have not been processed by Yang et al. (2007): 2 mergers, 3 S0 galaxies and 1 LTG.

23 (61%) of the galaxies with an off-centred weak [OIII] component are isolated, while 11 (29%) of those have counterparts (one of these is in the small cluster above mentioned), 4 (11%) have not been processed by Yang et al. (2007). Regarding galaxies with an off-centred strong [OIII] component, 4 (57%) of them are in isolated galaxies, and 1 (14%) in a pair of galaxies. The 2 (29%) remaining are not in Yang et al. (2007). Last, the majority 12 (92%) of galaxies with symmetrical kinematics are isolated and only 1 (8%) is in a pair.

2.5. Star formation

In Figure 5, we compute the stellar mass - sSFR diagram as discussed by Brinchmann et al. (2004) with stellar mass (resp. sSFR) computed by (Kauffmann et al. 2003) (resp. Brinchmann

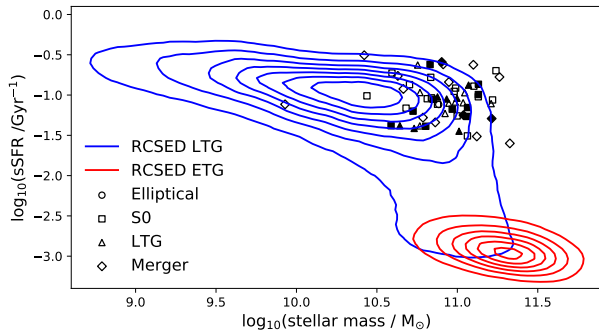


Fig. 5. Specific star formation rate (sSFR) (Brinchmann et al. 2004) as a function of stellar mass (Kauffmann et al. 2003). We compute as blue (resp. red) contour lines a sub-sample of LTG (resp. ETG) selected from the RCSED catalogue (Chilingarian et al. 2017). We display our galaxy sample with their morphology encoded in the marker style and highlight galaxies with off-centred weak [OIII] lines by empty marker.

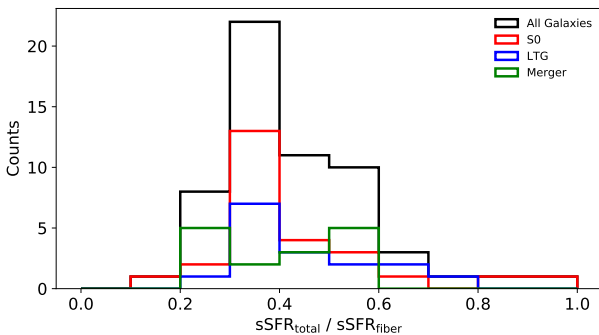


Fig. 6. Ratio of the total sSFR and the sSFR measured within the 3'' fibre by Brinchmann et al. (2004). The histogram is decomposed into different morphological types (2.2).

et al. (2004)). The galaxies from our sample are not quenched and exhibit a star formation ratio typical of the upper-mass range of the main sequence. In Figure 6, we present the ratio between the specific star formation ratio (sSFR) of the total galaxy and the sSFR of the 3'' SDSS fiber. The sSFR measurements are computed from Brinchmann et al. (2004). For all the galaxies, we observe a star formation stronger in the central regions.

We calculate the SFR from the extinction corrected H_{α} 6565 luminosity as described in Kewley et al. (2002). We compute the extinction for each line component using the Balmer decrements (Domínguez et al. 2013) assuming an intrinsic ratio $H_{\alpha}/H_{\beta} = 2.85$ (Osterbrock 1989) and the Whitford reddening curve from Miller & Mathews (1972). With the Balmer decrement, we estimate a mean $E(B-V)$ of 0.6 for the two peaks. The measured mean [OIII]/ H_{α} flux ratios of the weak and strong components are 0.2 and 1, while the differential dust attenuation between 5007Å and 6565Å is 0.7. Hence, the relative reduction of one of the [OIII] lines cannot be accounted for by extinction only. We subsequently compute the SFR following Kewley et al. (2002):

$$\text{SFR}(H_{\alpha})(M_{\odot}\text{yr}^{-1}) = 7.9 \cdot 10^{-42} L_{H_{\alpha}}(\text{erg s}^{-1}) \quad (1)$$

In Figure 7, we observe that the SFR associated to the strong [OIII] component is larger than the weak [OIII] one. This effect is even stronger for centred strong [OIII] components (discussed in Sect. 2.3) and especially for those which are also classified as composite (discussed in Sect. 2.1).

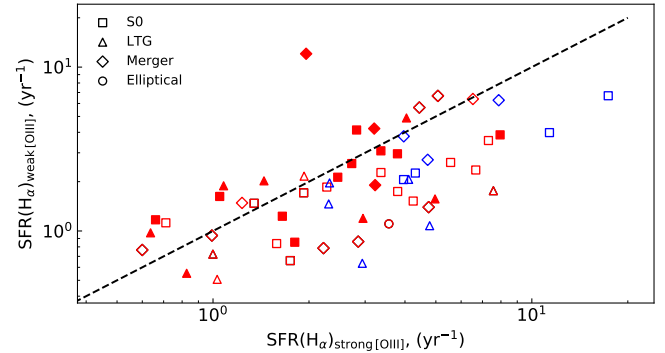


Fig. 7. Star formation ratio calculated from the extinction corrected H_{α} 6565 luminosity. On the x-axis (resp. y-axis), we display the SFR inferred from the strong [OIII] (weak [OIII]) component. We display the morphology (see Sect. 2.2) with different markers and indicate the BPT classification of the stronger [OIII] line as colour-coded in Figure 1. We highlight galaxies showing off-centred weak [OIII] lines with empty markers. The dashed line corresponds to equal SFR in the two components.

3. Discussion

The sample of emission-line galaxies discussed here exhibits two peaks lying in different regions of the BPT. We show that the gas velocities of the two peaks for only 22% of the galaxies are centred on the stellar velocity (see Fig. 4). All these galaxies exhibiting a symmetric kinematics are isolated but one (in a pair), and 69% of them are classified S0. This is not the expected proportion for the morphology of field disc galaxies (e.g. van den Bergh 2009). 78% of the galaxies have one gas peak associated to the stellar velocity, while the second one is offset. Only 33% of these galaxies with an offset kinematics are in pairs or small groups. All galaxies with the stronger [OIII] component classified as composite (see Figure 1) have a stellar velocity associated to this component (Figure 4).

We do not find any significant extinction bias between the two peaks, and the optical snapshots do not reveal any asymmetric features. Similarly, one might think of off-centred circum-nuclear discs like observed in NGC1068 (García-Burillo et al. 2017) or the off-centring of the AGN within the sphere of influence of the blackhole (Combes et al. 2019). However, it seems difficult to recover with a 3'' fiber these relatively small scale features. Again non-resolved triaxial structures or bars in the central regions might also produce a large velocity gradient and possibly a double peak feature, but it would be difficult to account for the observed off-centring of one component. In addition, this cannot account for the unusual morphological types of this sample.

On the one hand, half of the sample is composed of merger and late-type galaxies. As displayed in Figure 3, it is difficult to disentangle a double nucleus if the galaxy is distant. It is thus possible that the number of mergers is underestimated. On the other hand, half of the sample is composed of S0 galaxies. While the number of S0 is estimated larger in clusters of galaxies (28% according to van den Bergh (2009)), our sample is mainly composed of isolated galaxies or galaxies in small groups.

Those galaxies are actively forming stars: they lie in the upper-mass range of the star forming main sequence (see Figure 5). They are characterised by an enhanced star formation activity in their centre (see Figure 6). They also host an AGN. We find the SFR to be higher in the stronger [OIII] component (Figure 7). This effect is even more distinctive for strong [OIII] com-

ponents classified as composite which is counter intuitive since the weaker component is classified as SF.

Beside their morphological appearance, the S0 galaxies of this sample exhibit the same properties as the other galaxies of the sample. The origin of the S0 galaxies have been largely debated. While gas ejection by AGN has been proposed (e.g. van den Bergh 2009), it has also been shown that they could result from major/minor mergers (e.g. Eliche-Moral et al. 2018), which is supported here by the fact that some tidal features are observed around some of the S0 galaxies. These different points suggest that we might observe some mergers as well as ultimate phases of merging: galaxies with a double nucleus not resolved in the images or post-mergers (S0) with a central asymmetry. Fraser-McKelvie et al. (2018) discuss that large-mass S0 galaxies might be formed by mergers, as studied by Eliche-Moral et al. (2018). Given the known co-evolution of SF and accretion of the black hole, the AGN activity can be concomitant with an enhancement of SFR (e.g. Mihos & Hernquist (1994); Sancisi et al. (2008)).

Last, one can also discuss the possibility that the off-centred component is linked to an outflow of gas. Asymmetries in emission lines are known to be connected to gas outflow (Heckman et al. 1981; Whittle 1985). Such evidences are based on large field studies. Greene & Ho (2005) and Woo et al. (2016) used double Gaussian emission line structures in the [OIII] line only, while spectroscopic integral field unit studies show a difference in the velocity dispersion of the two lines (Sharp & Bland-Hawthorn 2010; Karouzos et al. 2016), which is not the case here. These observations are consistent with measured outflows creating high offset velocity dispersion of around 1300 km s^{-1} (Rupke & Veilleux 2013), even though smaller outflow velocities in the order of 100 km s^{-1} have been observed in NGC 5929 (Riffel et al. 2014) corresponding to double-peaks in the [OIII] line. We cannot exclude that our observations correspond to an outflow of gas which might explain an offset component.

4. Conclusion

We presented a sample of 58 double-peaked galaxies, displaying a single strong peak in the [OIII] $\lambda 5008$ corresponding to one of the $H_{\alpha}\lambda 6565$ components. The two components are classified differently according to the BPT diagnostics, with one peak corresponding to an AGN or a composite region and the second one in the composite or SF region. In addition, we observe an off-centring of one of the components with respect to the stellar velocity in 78% of the galaxies. In addition, these massive galaxies ($\sim 10^{11} M_{\odot}$) are actively forming stars with a central enhancement, and 45% of them are S0 galaxies. The large majority (67%) are isolated galaxies, while the others are hosted in small groups (with 2-5 galaxies), but one in a small cluster (of 27 galaxies). We can thus exclude this high fraction of S0 galaxies to be due to the environment. Given the galactic nuclei and star formation activities of these galaxies, we cannot exclude that we observe some gas outflows, which would require additional observations e.g. of molecular gas. In the meantime, it is probable that these kinematic signatures are linked to merging activity.

Acknowledgements. We thank Françoise Combes for interesting suggestions, and Gary Mamon for his support for this work. ALM has benefited from support from *Action Fédératrice "Cosmologie et Structuration de l'Univers"*. We thank the anonymous referee for constructive comments. Funding for the SDSS and SDSS-II has been provided by the Alfred P. Sloan Foundation, the Participating Institutions, the National Science Foundation, the U.S. Department of Energy, the National Aeronautics and Space Administration, the Japanese Monbukagakusho, the Max Planck Society, and the Higher Education Funding Council for England. The SDSS Web Site is <http://www.sdss.org/>. The Legacy Surveys (<http://legacysurvey.org/>) consist of three individual and

complementary projects: the Dark Energy Camera Legacy Survey (DECaLS; NOAO Proposal ID # 2014B-0404; PIs: David Schlegel and Arjun Dey), the Beijing-Arizona Sky Survey (BASS; NOAO Proposal ID # 2015A-0801; PIs: Zhou Xu and Xiaohui Fan), and the Mayall z-band Legacy Survey (MzLS; NOAO Proposal ID # 2016A-0453; PI: Arjun Dey). DECaLS, BASS and MzLS together include data obtained, respectively, at the Blanco telescope, Cerro Tololo Inter-American Observatory, National Optical Astronomy Observatory (NOAO); the Bok telescope, Steward Observatory, University of Arizona; and the Mayall telescope, Kitt Peak National Observatory, NOAO. The Legacy Surveys project is honoured to be permitted to conduct astronomical research on Iolkam Du'ag (Kitt Peak), a mountain with particular significance to the Tohono O'odham Nation.

References

- Baldwin, J. A., Phillips, M. M., & Terlevich, R. 1981, *PASP*, 93, 5
 Bell, E. F., Papovich, C., Wolf, C., et al. 2005, *ApJ*, 625, 23
 Bellocchi, E., Arribas, S., Colina, L., & Miralles-Caballero, D. 2013, *A&A*, 557, A59
 Bergvall, N., Laurikainen, E., & Aalto, S. 2003, *A&A*, 405, 31
 Brinchmann, J., Charlot, S., White, S. D. M., et al. 2004, *MNRAS*, 351, 1151
 Chilingarian, I. V., Zolotukhin, I. Y., Katkov, I. Y., et al. 2017, *ApJS*, 228, 14
 Cid Fernandes, R., Stasińska, G., Schlickmann, M. S., et al. 2010, *MNRAS*, 403, 1036
 Cid Fernandes, R., Stasińska, G., Mateus, A., & Vale Asari, N. 2011, *MNRAS*, 413, 1687
 Combes, F., García-Burillo, S., Audibert, A., et al. 2019, *A&A*, 623, A79
 Comerford, J. M., Nevin, R., Stemo, A., et al. 2018, *ApJ*, 867, 66
 Croton, D. J., Springel, V., White, S. D. M., et al. 2006, *MNRAS*, 365, 11
 Dey, A., Schlegel, D. J., Lang, D., et al. 2019, *AJ*, 157, 168
 Di Matteo, P., Combes, F., Melchior, A.-L., & Semelin, B. 2007, *A&A*, 468, 61
 Domínguez, A., Siana, B., Henry, A. L., et al. 2013, *ApJ*, 763, 145
 Domínguez Sánchez, H., Huertas-Company, M., Bernardi, M., Tuccillo, D., & Fischer, J. L. 2018, *MNRAS*, 476, 3661
 Eliche-Moral, M. C., Rodríguez-Pérez, C., Borlaff, A., Querejeta, M., & Tapia, T. 2018, *A&A*, 617, A113
 Fraser-McKelvie, A., Aragón-Salamanca, A., Merrifield, M., et al. 2018, *MNRAS*, 481, 5580
 García-Burillo, S., Viti, S., Combes, F., et al. 2017, *A&A*, 608, A56
 Ge, J.-Q., Hu, C., Wang, J.-M., Bai, J.-M., & Zhang, S. 2012, *ApJS*, 201, 31
 Greene, J. E., & Ho, L. C. 2005, *ApJ*, 627, 721
 Heckman, T. M., Miley, G. K., van Breugel, W. J. M., & Butcher, H. R. 1981, *ApJ*, 247, 403
 Kauffmann, G., Heckman, T. M., Tremonti, C., et al. 2003, *MNRAS*, 346, 1055
 Karouzos, M., Woo, J.-H., & Bae, H.-J. 2016, *ApJ*, 819, 148
 Kereš, D., Katz, N., Weinberg, D. H., & Davé, R. 2005, *MNRAS*, 363, 2
 Kewley, L. J., Dopita, M. A., Sutherland, R. S., Heisler, C. A., & Trevena, J. 2001, *ApJ*, 556, 121
 Kewley, L. J., Geller, M. J., Jansen, R. A., & Dopita, M. A. 2002, *AJ*, 124, 3135
 Kewley, L. J., Groves, B., Kauffmann, G., & Heckman, T. 2006, *MNRAS*, 372, 961
 Liu, X., Lazio, T. J. W., Shen, Y., & Strauss, M. A. 2018, *ApJ*, 854, 169
 Madau, P., & Dickinson, M. 2014, *ARA&A*, 52, 415
 McGaugh, S. S., Schombert, J. M., Bothun, G. D., & de Blok, W. J. G. 2000, *ApJ*, 533, L99
 Mihos, J. C., & Hernquist, L. 1994, *ApJ*, 425, L13
 Mihos, J. C., & Hernquist, L. 1996, *ApJ*, 464, 641
 Miller, J. S., & Mathews, W. G. 1972, *ApJ*, 172, 593
 Müller-Sánchez, F., Comerford, J. M., Nevin, R., et al. 2015, *ApJ*, 813, 103
 Nevin, R., Comerford, J. M., Müller-Sánchez, F., Barrows, R., & Cooper, M. C. 2018, *MNRAS*, 473, 2160
 Osterbrock, D. E. 1989, Research supported by the University of California, John Simon Guggenheim Memorial Foundation, University of Minnesota, et al. Mill Valley, CA, University Science Books, 1989, 422 p.,
 Patton, D. R., Torrey, P., Ellison, S. L., Mendel, J. T., & Scudder, J. M. 2013, *MNRAS*, 433, L59
 Riffel, R. A., Storch-Bergmann, T., & Riffel, R. 2014, *ApJ*, 780, L24
 Robaina, A. R., Bell, E. F., Skelton, R. E., et al. 2009, *ApJ*, 704, 324
 Rupke, D. S. N., & Veilleux, S. 2013, *ApJ*, 768, 75
 Sancisi, R., Fraternali, F., Oosterloo, T., & van der Hulst, T. 2008, *A&A Rev.*, 15, 189
 Sanders, D. B., & Mirabel, I. F. 1996, *ARA&A*, 34, 749
 Satyapal, S., Ellison, S. L., McAlpine, W., et al. 2014, *MNRAS*, 441, 1297
 Schawinski, K., Thomas, D., Sarzi, M., et al. 2007, *MNRAS*, 382, 1415
 Sharp, R. G., & Bland-Hawthorn, J. 2010, *ApJ*, 711, 818
 Springel, V., Di Matteo, T., & Hernquist, L. 2005, *MNRAS*, 361, 776
 Strauss, M. A., Weinberg, D. H., Lupton, R. H., et al. 2002, *AJ*, 124, 1810
 Yang, X., Mo, H. J., van den Bosch, F. C., et al. 2007, *ApJ*, 671, 153
 Whittle, M. 1985, *MNRAS*, 213, 1
 van den Bergh, S. 2009, *ApJ*, 702, 1502
 Woo, J.-H., Bae, H.-J., Son, D., & Karouzos, M. 2016, *ApJ*, 817, 108

Appendix A: Additional figures

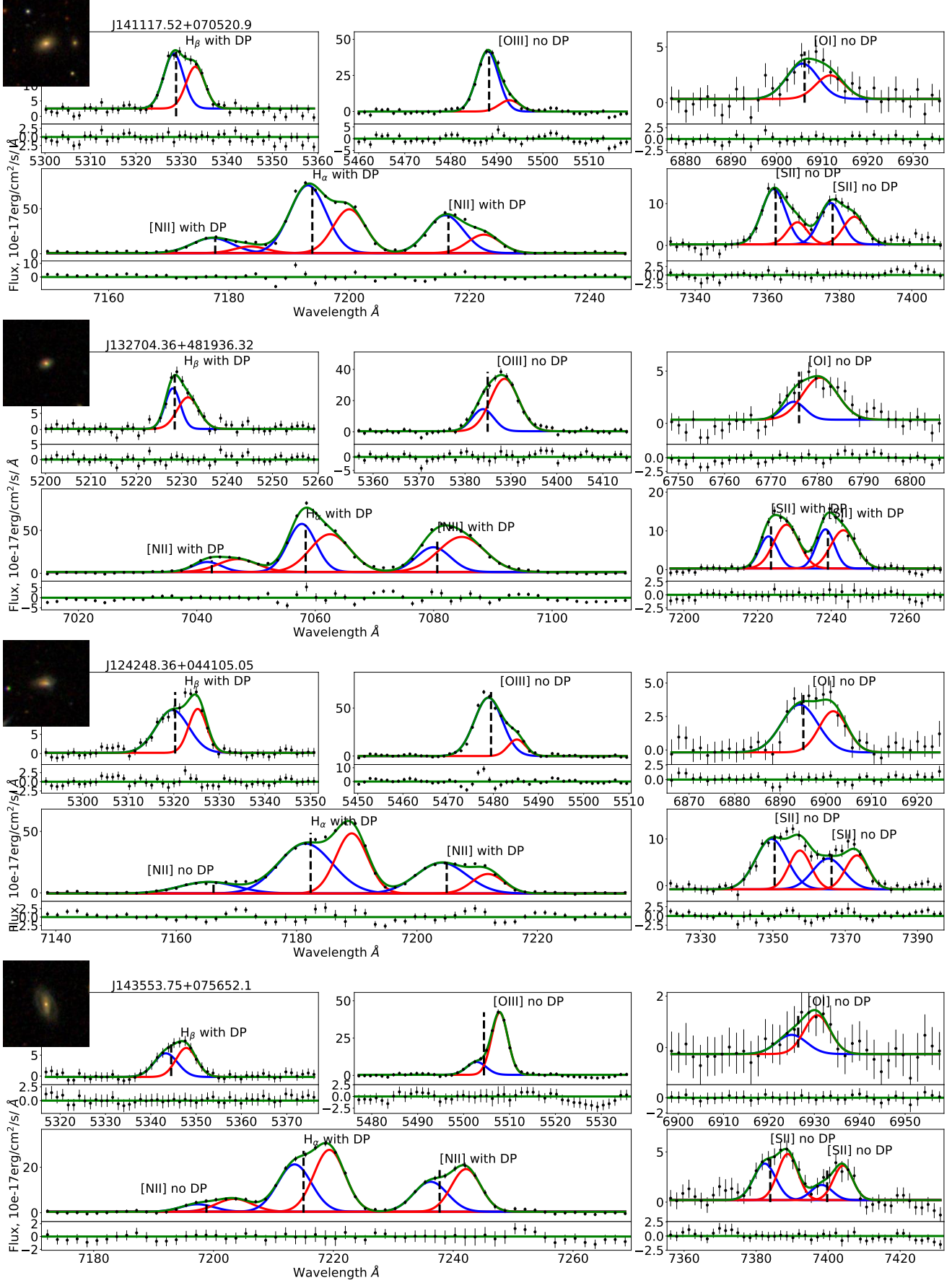


Fig. A.1. Emission lines of other representative double-peak galaxies. The first two figures, on the top, are classified S0 while the last two figures correspond to LTG. Same colour coding as in Fig. 2.

ID	Designation	z	$\phi_s^{[OIII]} / \phi_w^{[OIII]}$	Morph	BPT [OIII] _s	BPT [OIII] _w	WHAN [OIII] _s	WHAN [OIII] _w	Kin	N _g
(1)	(2)	(3)	(4)	(5)	(6)	(7)	(8)	(9)	(10)	(11)
1	J154403.67+044610.08	0.042	4.8 ± 0.7	<i>Merger</i>	LINER	SF	sAGN	sAGN	off-w	4
2	J075416.45+200136.32	0.046	65.0 ± 58.7	LTG	COMP	SF	sAGN	SF	off-w	2
3	J091954.54+325559.79	0.049	7.9 ± 2.0	<i>Merger</i>	COMP	SF	sAGN	SF	off-w	0
4	J142859.54+605000.58	0.052	13.4 ± 7.6	S0	LINER	COMP	wAGN	wAGN	cen	1
5	J143555.01+103117.22	0.055	4.6 ± 1.2	LTG	AGN	COMP	wAGN	wAGN	off-s	1
6	J143454.41-011618.06	0.056	3.8 ± 0.6	S0	AGN	COMP	sAGN	wAGN	cen	1
7	J084810.10+351534.05	0.057	12.5 ± 1.9	<i>Merger</i>	AGN	COMP	sAGN	sAGN	off-w	0
8	J120923.63+620955.96	0.060	9.3 ± 3.0	S0	LINER	COMP	wAGN	wAGN	off-w	1
9	J233141.99-103206.95	0.061	3.8 ± 1.1	S0	LINER	COMP	wAGN	wAGN	cen	1
10	J001119.84-093940.57	0.062	79.5 ± 30.0	LTG	AGN	SF	sAGN	RG	off-w	1
11	J083515.21+511732.70	0.067	5.0 ± 1.6	<i>Merger</i>	AGN	SF	sAGN	sAGN	off-w	1
12	J153556.76-013749.17	0.070	32.6 ± 23.4	S0	AGN	COMP	sAGN	wAGN	off-w	1
13	J095600.70+130806.78	0.070	15.9 ± 6.7	LTG	COMP	SF	sAGN	SF	off-w	2
14	J110233.35+224513.71	0.074	16.6 ± 10.0	LTG	LINER	COMP	wAGN	RG	off-w	1
15	J164754.90+443345.05	0.074	16.3 ± 7.1	S0	COMP	SF	sAGN	sAGN	off-w	4
16	J142457.53+241517.82	0.075	4.4 ± 0.9	S0	AGN	COMP	wAGN	wAGN	off-w	2
17	J132704.36+481936.32	0.076	3.1 ± 0.6	S0	AGN	COMP	sAGN	sAGN	off-w	1
18	J142606.64+202831.56	0.077	6.8 ± 2.8	<i>Merger</i>	COMP	SF	sAGN	SF	off-w	4
19	J081204.73+171703.77	0.081	4.0 ± 0.9	S0	AGN	COMP	sAGN	sAGN	cen	1
20	J121446.40+013547.43	0.083	8.1 ± 3.1	S0	AGN	COMP	wAGN	wAGN	off-w	1
21	J015415.01+144716.78	0.084	10.8 ± 5.0	Ellip	AGN	COMP	sAGN	wAGN	off-w	1
22	J165253.53+324440.29	0.086	13.5 ± 3.7	<i>Merger</i>	AGN	COMP	sAGN	wAGN	off-w	2
23	J090012.03+450514.82	0.088	43.3 ± 39.3	S0	COMP	SF	sAGN	SF	off-w	27
24	J073420.09+284038.96	0.089	151.7 ± 136.7	LTG	COMP	SF	sAGN	sAGN	off-w	1
25	J093805.80+270456.72	0.090	3.6 ± 0.7	LTG	AGN	COMP	sAGN	sAGN	cen	1
26	J131943.32+515255.83	0.090	5.1 ± 1.5	LTG	AGN	COMP	sAGN	sAGN	off-s	2
27	J075932.35+193325.57	0.093	15.0 ± 7.3	S0	AGN	COMP	wAGN	RG	cen	1
28	J143035.27+443825.35	0.093	9.8 ± 3.7	LTG	COMP	SF	sAGN	wAGN	off-w	1
29	J154124.59+271508.18	0.094	9.8 ± 3.8	S0	LINER	COMP	sAGN	wAGN	off-w	1
30	J124248.36+044105.05	0.094	5.6 ± 0.4	LTG	AGN	COMP	sAGN	SF	off-w	1
31	J100759.81+630128.97	0.095	3.1 ± 0.6	LTG	AGN	COMP	wAGN	sAGN	off-s	1
32	J141117.52+070520.89	0.096	5.6 ± 1.5	S0	AGN	SF	sAGN	wAGN	off-w	1
33	J143553.84+075652.13	0.099	4.0 ± 1.1	LTG	AGN	COMP	wAGN	wAGN	cen	1
34	J113914.89-024107.87	0.103	3.4 ± 1.0	<i>Merger</i>	LINER	COMP	sAGN	wAGN	off-w	1
35	J103554.15+110243.16	0.105	8.5 ± 1.3	<i>Merger</i>	AGN	SF	sAGN	sAGN	off-w	2
36	J144222.93+580434.42	0.105	4.8 ± 1.7	S0	COMP	SF	sAGN	SF	off-w	1
37	J075016.22+145816.70	0.107	4.0 ± 1.3	S0	LINER	COMP	sAGN	sAGN	off-w	0
38	J080738.22+504526.08	0.120	13.9 ± 6.3	<i>Merger</i>	COMP	SF	sAGN	sAGN	off-w	1
39	J154447.10+462817.72	0.121	6.4 ± 1.6	S0	AGN	COMP	sAGN	wAGN	cen	1
40	J142404.89+183606.76	0.121	4.0 ± 1.1	S0	AGN	SF	wAGN	sAGN	cen	1
41	J165742.02+380058.76	0.122	5.3 ± 1.0	<i>Merger</i>	AGN	SF	sAGN	sAGN	off-s	1
42	J091431.22+551020.47	0.123	4.7 ± 1.2	S0	AGN	COMP	wAGN	wAGN	cen	1
43	J090211.82+083609.82	0.128	3.5 ± 1.1	LTG	AGN	COMP	sAGN	sAGN	off-s	0
44	J164507.91+205759.50	0.130	3.3 ± 0.6	<i>Merger</i>	AGN	COMP	sAGN	sAGN	cen	2
45	J164048.18+420042.75	0.133	25.7 ± 10.2	S0	AGN	SF	sAGN	sAGN	off-w	2
46	J090308.54+272639.04	0.135	3.3 ± 0.9	<i>Merger</i>	AGN	COMP	sAGN	sAGN	off-w	1
47	J131044.32+245650.58	0.136	74.0 ± 29.6	LTG	COMP	SF	sAGN	wAGN	off-w	1
48	J103510.83+420935.01	0.137	10.4 ± 4.0	S0	COMP	SF	sAGN	SF	off-w	1
49	J164155.60+252952.38	0.137	8.6 ± 3.6	LTG	AGN	COMP	sAGN	wAGN	off-w	1
50	J105546.75+055409.21	0.138	8.1 ± 3.5	S0	LINER	COMP	sAGN	wAGN	off-w	1
51	J161050.02+324000.60	0.140	14.9 ± 7.7	S0	AGN	COMP	sAGN	wAGN	off-w	5
52	J104903.68+253323.97	0.140	3.1 ± 0.6	LTG	AGN	COMP	wAGN	sAGN	off-s	1
53	J074715.76+370649.32	0.140	4.0 ± 0.9	<i>Merger</i>	AGN	COMP	sAGN	sAGN	cen	1
54	J103945.99+173849.13	0.143	6.9 ± 2.4	S0	AGN	COMP	sAGN	sAGN	off-w	0
55	J171731.31+282424.67	0.152	6.6 ± 2.2	S0	AGN	COMP	sAGN	sAGN	cen	1
56	J150552.72+192909.16	0.157	6.2 ± 2.0	<i>Merger</i>	LINER	COMP	sAGN	sAGN	off-w	1
57	J093610.57+303130.25	0.162	17.7 ± 11.8	<i>Merger</i>	AGN	SF	sAGN	sAGN	off-w	1
58	J141426.56+643540.20	0.166	5.3 ± 1.8	S0	AGN	SF	sAGN	sAGN	off-s	0

Table A.1. Merger candidates sorted by redshift. (2) SDSS designation, (3) SDSS redshift in the third column, (4) [OIII] λ 5008 ratio between the strong [OIII] and weak [OIII] line component, (5) morphological classification, (6) and (7) BPT diagram classification for strong (s) and weak (w) [OIII] peak (Figure 1), (8) and (9) WHAN diagram classification for each peak, (10) kinematic classification of the gas emission line components with respect to the stellar velocity: ‘off-s’ (resp. ‘off-w’) off-centred strong (resp. weak) [OIII] component and ‘cen’ for centred [OIII] line components (see 2.3), (11) number of identified galaxies in the corresponding group (Yang et al. 2007), 0 is provided when the galaxy has not been processed.

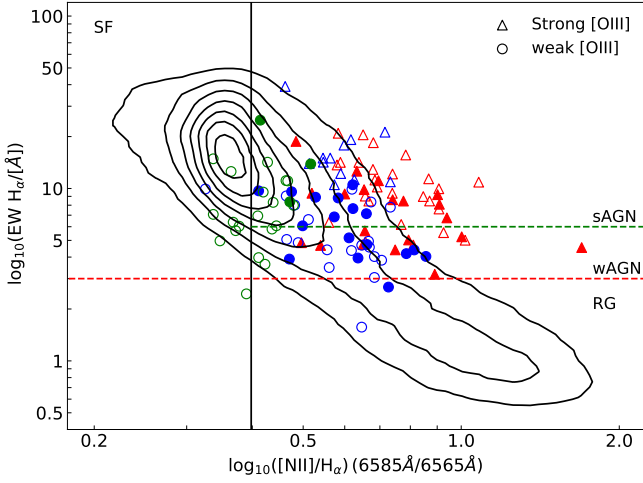


Fig. A.2. The diagnostic diagram introduced by Cid Fernandes et al. (2010) as an alternative to the BPT classification (see Figure 1). A topological separation classifies galaxies into star forming galaxies (SF), strong and weak AGNs (sAGN and wAGN) and retired galaxies (RG) (Cid Fernandes et al. 2011). We compute the two double-peak components of the merger candidates individually: we display the component dominating the [OIII] λ 5008 line as triangles and the suppressed component as circles. We adapt the colour-coding according to the BPT classification in Figure 1. We highlight galaxies with off-centred weak [OIII] lines by empty markers (2.3) We observe that the majority of our classified components are situated in the AGN region. We recognise a shift between the two components which correlates with the [OIII] λ 5008 strength. The component dominating the [OIII] is more likely classified as sAGN (45) and only some as wAGN (13). The suppressed [OIII] component shows 26 sAGNs, 21 wAGNs 8 SF and 4 RG.